Journal of Environmental Chemical Engineering 12 (2024) 113372

Contents lists available at ScienceDirect

Journal of Environmental Chemical Engineering

journal homepage: www.elsevier.com/locate/jece

Experimental investigation of photo-thermal catalytic reactor for the reverse water gas shift reaction under concentrated irradiation

David Brust [a,*], Michael Wullenkord [a], Hermenegildo García Gómez [b], Josep Albero [b], Christian Sattler [a]

[a] German Aerospace Center (DLR) - Institute of Future Fuels, Linder Höhe, Köln 51147, Germany
[b] Instituto Universitario de Tecnología Química (CSIC-UPV), Universitat Politècnica de València, Avda. De los Naranjos, Valencia 46022, Spain

ARTICLE INFO

Keywords:
Photo-thermal catalysis
Reverse water gas shift
Concentrated irradiation
Solar simulator
Modelling

ABSTRACT

An upscaled photo-thermal catalytic reactor for the heterogeneously catalysed reverse Water Gas Shift (rWGS) reaction is tested under simulated concentrated irradiation. The reactor is equipped with an aperture of 144 cm^2 area covered by a quartz window, where it receives irradiation flux densities of up to 80 kW/m^2 corresponding to an irradiation power input of 1 kW thereby directly irradiating a RuO_2 based photo-thermal catalyst that is deposited on a porous support. The system was operated under simulated concentrated sunlight for a total of 45.5 h with 35.4 h of chemical operation. A peak CO production rate of 1.6 mol/h was achieved with an average light concentration factor of 80 in the centre of the catalyst layer. This corresponds to a solar-to-chemical efficiency – defined by the ratio of the product of molar CO production rate and reaction enthalpy for the rWGS reaction and the irradiation power input – of 1.69 %. A calculation approach to determine the catalyst surface temperature under irradiation was introduced and utilised for performance analysis leading to the discussion of design modifications and operating strategies towards performance enhancement.

1. Introduction

In recognition of the facts that anthropogenic emissions of greenhouse gases are the main driver of the currently observable climate change [1] and that the chemical industry in particular contributed roughly 7 % to the total global greenhouse gas emissions in 2018 [2], research efforts towards the reduction of its carbon dioxide (CO_2) emissions are pursued to reduce the environmental impact of chemicals production. Photo-thermal catalysis is emerging as an innovative approach which aims at the utilisation of (solar) light energy to catalyse chemical reactions. Depending on the type of reaction, this constitutes a process that converts light energy to chemical energy and thus stores light energy in the form of feedstock chemicals [3] potentially offering pathways to lower CO_2 emissions from the chemical industry. Photo-thermal catalysis employs a wide range of material combinations where transition metals like Ni, Cu or Ru paired with metal oxide semiconductors like Al_2O_3, TiO_2 or $SrTiO_3$ are common choices [4]. Among other reactions, photo-thermal catalysis has been applied in methane dry reforming, ammonia decomposition, CO_2 reduction and hydrogenation to methanol and the reverse Water Gas Shift (rWGS) reaction [3].

The latter is a promising application of CO_2 utilization [5] and offers an alternative pathway towards synthesis gas (syngas) production: Syngas, a mixture of hydrogen (H_2) and carbon monoxide (CO) in different proportions is an important intermediate product of chemical industry used for methanol and Fischer-Tropsch syntheses as well as hydroformylation [6]. Presently, syngas is predominantly derived from various carbon containing feedstocks, which can be any fossil fuel or biomass. When fossil feedstocks are utilized, syngas production is associated with a high carbon intensity.

When H_2 from carbon-free sources reacts with CO_2 in the endothermic rWGS reaction to form CO with water (H_2O) as by-product (1), syngas can be produced via a fossil-free pathway [5].

$$\text{rWGS}: \quad CO_2 + H_2 \rightleftharpoons CO + H_2O, \quad \Delta h^0_{rWGS} = 41.2 \text{kJ/mol} \tag{1}$$

Published Life-Cycle Analyses (LCA) reveal that a process for syngas production using H_2 and energy input from carbon-free sources based on the rWGS reaction has a large potential for the reduction of greenhouse gas emissions [5]. In light of this, the idea of using solar energy input to drive the endothermic rWGS reaction has increasingly gained attention [7–9].

* Corresponding author.
E-mail address: david.brust@dlr.de (D. Brust).

https://doi.org/10.1016/j.jece.2024.113372
Received 31 January 2024; Received in revised form 13 June 2024; Accepted 17 June 2024
Available online 18 June 2024

Utilization of solar energy through the rWGS reaction can be achieved via plasmonic catalysis [10]. A commonly investigated plasmonic catalyst for the rWGS reaction is Au-TiO_2. In [11] a lab scale flow reactor with Au-TiO_2 catalyst was operated with concentrated light corresponding to 5 suns and at temperatures up to 400 °C. A mechanism for the light enhancement of the rWGS reaction was proposed and reaction rate expressions were derived based on the proposed mechanism. Another study investigated the Au-TiO_2 plasmonic catalyst for the low-temperature reduction of CO_2 towards CO with concentrated light of up to 14.4 suns in a batch reactor [12]. It was concluded that with irradiation the selectivity towards CO increases compared against reference experiments in the dark at the same temperature. In a recent study, the same group tested the Au-TiO_2 catalyst for the rWGS reaction in an upscaled reactor in flow configuration [13]. In line with the previous study, the flow reactor was operated at 3.5 bar_g with solar simulated light of up to 14.4 suns of concentration. In this study no external heating was applied. The feed was varied in the range of molar compositions from $H_2/CO_2 = 1/1$ to 1/7 where the maximum CO productivity was observed at a molar feed ratio of $H_2/CO_2 = 1/4$ with a CO production rate of 7420 mmol/(m^2 h) at >96 % selectivity towards CO. Despite the claims of Au-TiO_2 being a plasmonic catalyst, the authors attributed the catalytic activity upon irradiation mostly to photo-thermal heating [13]. Another group also studied the size effects of Au-TiO_2 nanoparticles on activity and selectivity in the rWGS reaction at temperatures up to 160 °C and pressures up to 3.5 bar_g [14]. It was found that smaller particles displayed higher activity, beyond the expected increase in activity resulting from a larger specific surface area when using smaller particles.

In [15] the gas-phase hydrogenation of CO_2 on In_2O_3 was studied. It was observed that both an increase in temperature as well as light irradiation facilitate the conversion rate. When operating a laboratory scale continuous flow reactor at 1 mL/min of a $H_2/CO_2 = 1/1$ mixture at temperatures up to 300 °C with an irradiation concentration of around 8 suns from a 300 W Xe lamp, exclusive selectivity towards CO was achieved. In [16] a photo-thermal catalyst consisting of $Ni_{12}P_5$ nanoparticles in core-shell structure supported on silica was studied for the rWGS reaction under concentrated irradiation. A continuous flow reactor was operated without external heating at atmospheric pressure with a feed mixture of $CO_2/H_2/N_2 = 1/1/2$ at irradiation concentrations up to 40 suns from a 300 W Xe arc lamp. The resulting temperature when operating at 40 suns without external heating was estimated at 426 °C. For the investigated feed rates, a near complete selectivity towards CO was achieved.

The possibility that concentrated light irradiation on suitable catalysts consisting of metal and oxide semiconductor pairs can cause further non-thermal phenomena besides the light-induced heating effect, which then lead to the increase of reaction rates as well as changes in selectivity [4] holds promise for this class of catalysts as well as merits further research to discern the phenomena that can occur simultaneously.

While this study does not attempt to discover the catalytic mechanism and the processes occurring on the catalyst following from concentrated light irradiation leading to the observed conversion of CO_2 with H_2 in the rWGS reaction, this study reports on the design and experimental assessment of a novel, upscaled photo-thermal catalytic reactor that was tested with a concentrated irradiation power input of up to 1 kW to perform the rWGS reaction. The gas phase reactants H_2 and CO_2 were premixed and fed in continuous flow via a side port to the reactor whose quartz window received the concentrated irradiation. A RuO_2 based photo-thermal catalyst [17] was immobilized on a porous support structure positioned in the light path behind the window. It received the concentrated irradiation directly and catalysed the rWGS reaction via heterogenous catalysis where the active species under operation conditions was suspected to be Ru(0).

Beginning with an introduction to the design and working principle of the photo-thermal catalytic reactor, the catalyst synthesis is briefly outlined, followed by the characterisation of optical properties of the deposited catalyst. An overview on the experimental setup including the optical system consisting of the solar simulator as well as light guiding and irradiation shielding installations is given. Next, the supporting system necessary to operate and monitor the reactor, i.e. piping and instrumentation components, are briefly outlined. The following theoretical section focuses on a calculation-based approach aiming at obtaining the effective catalyst surface temperature during operation while also providing insights on sensitivity with respect to input parameters and uncertainty characterisation. The results section firstly reports on the experimentally realised irradiation fluxes, which are a determining input parameter for reactor operation. Then, an overview over the applied operating conditions over the course of the experimental campaign is given, followed by results of experimental testing separated into thermal and chemical evaluation. The chemical process occurring during reactor operation under a broad range of operating conditions is analysed and a measure for solar-to-chemical efficiency is proposed and applied.

The experimentally observed performance of the photo-thermal catalytic reactor is summarized by reporting on productivity, product composition and chemical conversion. The work concludes by summarising the most important findings and giving an outlook on future work.

2. Materials and methods

2.1. Photo-thermal catalytic reactor

The photo-thermal catalytic reactor is engineered for continuous flow operation at nearly atmospheric pressure, accommodating flow rates of up to 5.6 L_s/min. The reactor is composed of two compartments divided by a porous quartz plate, as illustrated in Fig. 1.

The primary structure of the reactor comprises two concentric squares, measuring 120 and 161 mm, respectively, and constructed from Aluminium 6082 (Fig. 1d). A porous plate with a square shape (158 mm side, 4 mm thick) is positioned inside the reactor's main body, held in place by the smaller reactor square. This porous support not only divides the reactor into two chambers but also serves as the platform for catalyst support (Fig. 1a). A square frame is employed to secure the porous support between the reactor lid and the main body (Fig. 1c). The reactor lid features a quartz window measuring 138 mm on each side and 5 mm in thickness (Fig. 1b). Finally, an Aluminium plate with a side length of 190 mm is used to close the bottom part of the reactor (Fig. 1e).

The gas mixture enters the upper chamber of the reactor, positioned between the quartz window and the porous plate coated with the catalyst (Fig. 2). It traverses the porous plate in close proximity to the catalysts and exits the reactor from the bottom chamber. Connections for gas inlet and outlet, as well as thermocouple ports, are located on the sides of the reactor.

2.2. Photo-thermal catalyst

The catalyst was prepared following the previously reported procedure [17]. In a nutshell, a mixture of $RuCl_3 \cdot x\, H_2O$, commercial $SrTiO_3$ nanoparticles from Sigma-Aldrich, and ethylene glycol was heated at 180 °C for 8 hours. Subsequently, after washing and drying, the resulting solids underwent calcination at 350 °C for 2 hours. The catalyst was applied through spray coating onto the porous quartz support, achieving a final loading of 3.5 mg/cm^2. This method ensured a uniform coating across the surface of the porous support, penetrating only ca. 300 μm, as depicted in Figure S 1.

Initially, the catalyst was deposited on glass fibre sheets shown in Figures S 6a and b to allow a faster exchange of the catalyst coated material and thus to facilitate variation of catalyst mass loading. The deposition utilizing glass fibre sheets was only used during pre-tests in inert atmosphere as the glass fibre sheets suffered from limited thermal stability. For the experiments fed with H_2/CO_2 mixtures presented in Section 4.2 the catalyst was directly deposited on a porous sintered glass

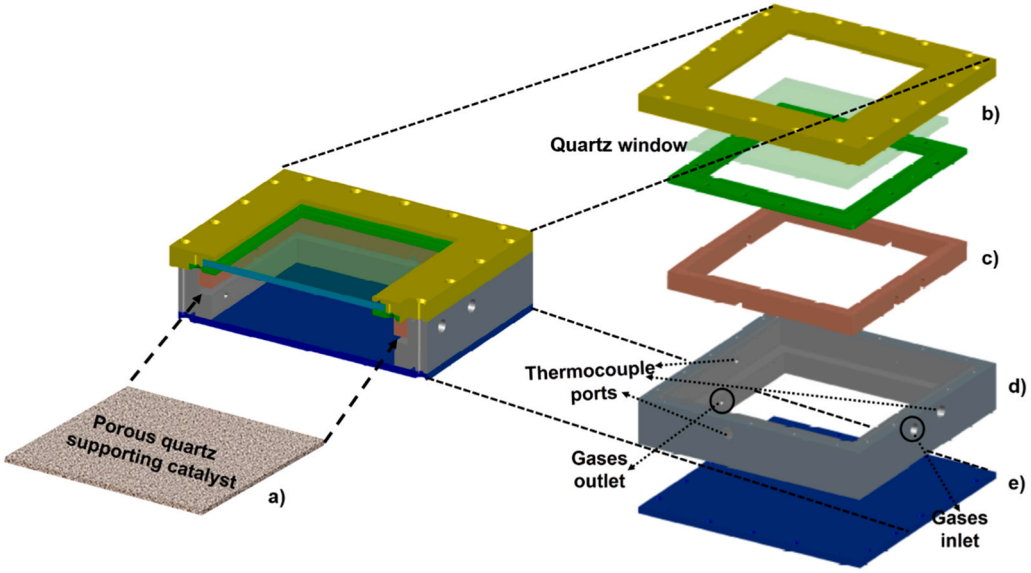

Fig. 1. Schematic illustration of the photo-thermal reactor.

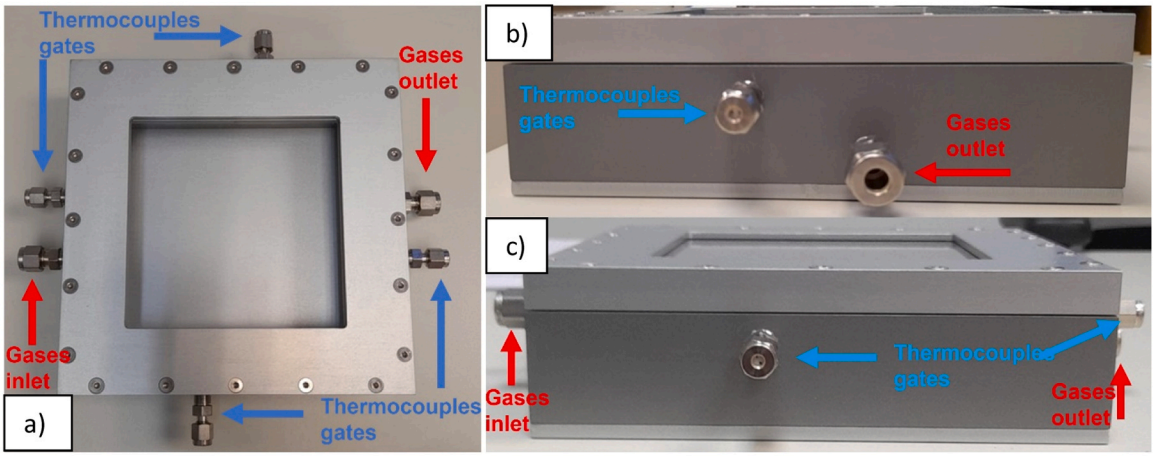

Fig. 2. Images of the photo-thermal reactor from a) the top, b) the right side and c) the front side highlighting the locations of gas inlet, outlet, and thermocouple ports.

frit which displayed better thermal stability shown in Figures S 1 and S 2 c.

2.3. Catalyst characterisation

The total loading of Ru on the catalyst was investigated by X-ray fluorescence spectroscopy resulting in a total loading of 2.5 wt%. The particle size distribution has been estimated after measurement of a statistically relevant number of nanoparticles from TEM images. Fig. 3 shows a representative TEM image including particle size distribution. As can be observed, the average particle size was 4.7 ± 1.1 nm.

The Ru oxidation state under reaction conditions has previously been determined using in situ Raman and SPC spectroscopy [17]. It was reported that at temperatures as low as 100 °C, Ru oxide species are reduced to Ru metal under H_2 atmosphere. Therefore, we assume that under the reaction conditions of our present work, which involve concentrated irradiation of up to 80 suns applied to the catalyst, the active species during operation is Ru(0).

Samples of the catalyst coated glass fibre sheets with a total catalyst mass loading of 100 mg dispersed on an area of 10 cm×10 cm were analysed with respect to their optical properties in the UV/Vis and IR ranges while being subjected to elevated temperatures up to 500 °C. The hemispherical reflectance was obtained in the wavelength range between 250 nm and 2500 nm (Perkin Elmer Lambda 950) with a modified sample holder allowing for heating the sample up to 500 °C during measurements [18]. In the NIR – IR spectral range the hemispherical directional reflectance was measured by a Nicolet FTIR

6700 spectrophotometer coupled to a SOC-100 HDR reflectometer (Surface Optics Corporation). The SOC-100 HDR is also equipped with a sample heater that allows heating the sample up to 500 °C.

The resulting reflectance spectra obtained at temperatures from room temperature to 500 °C in the UV/VIS and NIR/IR spectral ranges were then weighted by the spectrum of the Xe short arc based solar simulator (Osram XBO®) for the UV/VIS range and by a black-body spectrum at 600 °C for the NIR/IR range to obtain effective values for reflectance in the respective spectral ranges. Fig. 4 shows the resulting effective reflectance values of the catalyst coated glass fibre sheets at different temperatures and a comparison with a room temperature measurement after the heating to see if irreversible changes have occurred.

For the UV/VIS spectral range a value of 62 % for the reflectance was found over the whole temperature range with no irreversible changes

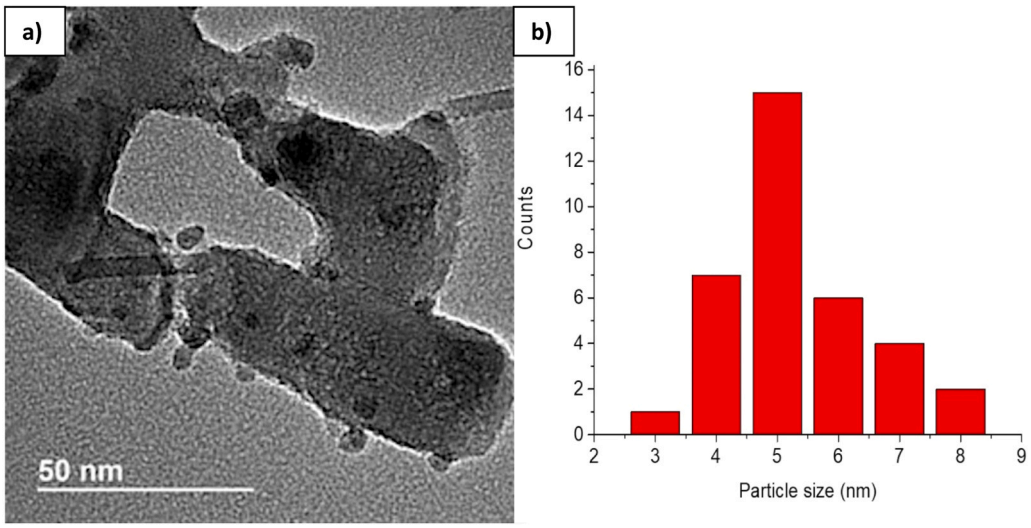

Fig. 3. TEM image of RuO_2-$SrTiO_3$ catalyst, showcasing RuO_2 nanoparticles with an average size of 4.7 ± 1.1 nm (a) and corresponding histogram of RuO_2 nanoparticle size distribution (b).

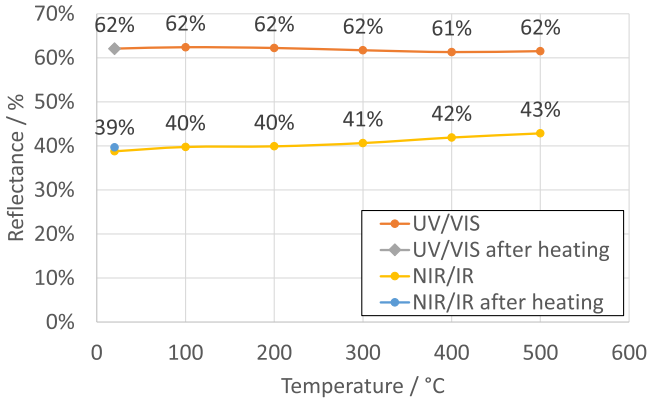

Fig. 4. Effective reflectance values obtained from spectral weighting with the spectrum of the Xe short arc based solar simulator for the UV/VIS range and with a black-body spectrum at 600 °C for the NIR/IR range, respectively.

due to the heating. For the NIR/IR range a linear increase in reflectance from 39 % at room temperature to 43 % at 500 °C was observed which was not fully reversible since a room temperature measurement after the heating revealed a reflectance in the NIR/IR spectrum of 40 %. For completeness, the reflectance spectra are shown in Figure S 3.

2.4. Experimental setup

The operation and experimental assessment of the reactor requires the handling of input and output material streams, power input to drive the endothermic rWGS reaction as well as measurement instrumentation including temperature and pressure sensors as well as product analysis.

2.4.1. Development of optics and optical qualification measurements

The photo-thermal catalytic reactor utilises concentrated solar irradiation as power input. Throughout this study the reactor was operated with an artificial light source, which imitates the characteristics of concentrated solar light [19]. The artificial light source is based on 10 Xenon short arc lamps equipped with ellipsoidal reflectors. It can focus irradiative power of up to 25 kW onto a focal spot of 100 cm^2 area in a distance of 3 m.

In addition, supporting optical components are required to transport the concentrated light from the light source to the reactor aperture and to control the light characteristics of the incident light on the catalyst layer in accordance with the design requirements. Iteratively, a suitable optical system was established. It comprises a water-cooled flux guide and a scattering window as well as diverse irradiation protection plates as can be seen in Fig. 5.

During pre-tests with a smaller version of the reactor, it was determined to consider irradiation flux densities up to 100 kW/m^2 corresponding to 100 suns of concentrated sunlight. As described in Section 2.1, the reactor is equipped with an aperture of 12 cm×12 cm. To completely utilize the photo-thermal catalyst, a very homogeneous flux profile in the catalyst plane is desired. To this end, a square of 10 cm×10 cm in the centre of the catalyst coated frit is designated as the "core" area for which nominal irradiation flux densities in the range from 40 to 80 kW/m^2 are specified. To realise this range of flux densities on a total illuminated area of 12 cm×12 cm, two lamps were required and the flux was controlled by adjusting the lamp current.

To obtain the effective flux density profile in the plane of the catalyst layer, a high-resolution optical measurement system [20] was applied to a reactor placeholder, that was mounted at the same position as the reactor. The placeholder replicates the geometry of the photo-thermal catalytic reactor including the quartz window and allows determining the effective flux density profile incident on the catalyst plane. In this instance, a variation of the optical measurement system including a transmissible target was employed. It allowed to apply the flux measurement system based on the "camera-target" method [20] from the backside as the front side is occupied by the optical installation shown in Fig. 5. Results for flux density measurements are reported in Section 4.1.

2.4.2. Piping and instrumentation

Reactor operation including safety monitoring and data acquisition require supporting infrastructure in the form of instrumentation and piping to provide feed and purge gases as well as to remove the product gases. To this end, a simplified scheme of the reactor, feed and gas analysis is shown in Fig. 6, while the complete piping and instrumentation diagram (P&ID) for the experimental setup is shown in the supplemental information in Figure S 4.

In particular, the gas phase reactants H_2 and CO_2 were supplied by mass flow controllers (max. flow 10,000 sccm, Bronkhorst). For testing with inert atmosphere, an additional N_2 feed was provided (max. flow 1000 sccm, Bronkhorst). The feed gas stream could be pre-heated before entering the reactor. After passing through the reactor, the product gas mixture was cooled, passed through a filter and was dried before entering a gas phase chromatograph (490 Micro GC, Agilent) for

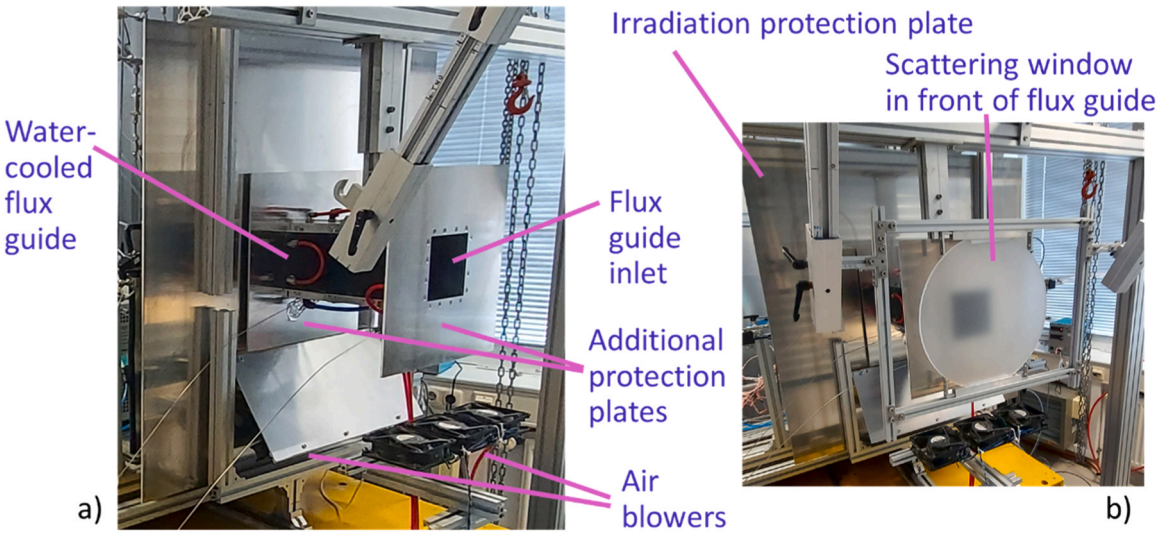

Fig. 5. Main parts of the developed optics: a) without and b) with scattering window in front of flux guide inlet.

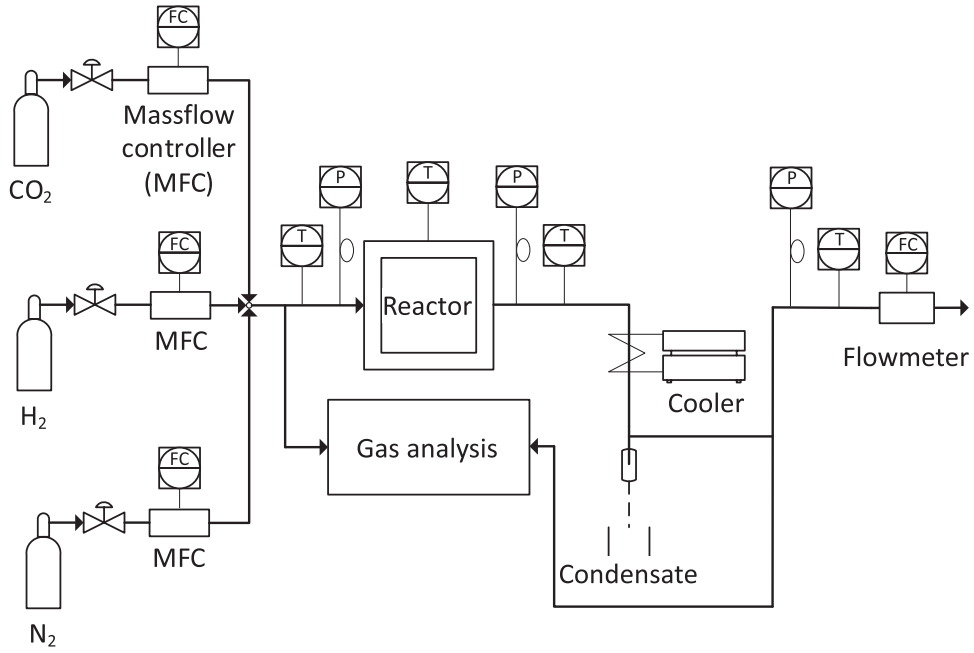

Fig. 6. Simplified schematic of the piping and instrumentation used for the operation of the photo-thermal catalytic reactor.

analysis. An additional flow of N_2 controlled by a mass flow controller (max. flow 500 sccm, MKS) could be fed into the product line before entering gas analysis to facilitate the calculation of molar product flows.

The reactor temperature was monitored via thermocouples (Type N) including feed and exhaust gas temperatures placed inside and outside of the reactor. The thermocouple placement and numbering are shown in the supplemental information in Figure S 5 for the upper chamber and Figure S 6 for the lower chamber of the reactor.

The gas pressure was measured with pressure sensors (WIKA S-11) upstream and downstream the reactor to ensure safe operation within the allowed limits and determination of the pressure drop over the reactor. In addition, the pressure was measured upstream of the float-type flow-meters (MR3000, Key Instruments) in the exhaust line.

3. Calculation

The surface temperature of the catalyst that establishes during operation under simulated concentrated sunlight is the dominant factor influencing the rate of the catalytic reaction for photo-thermal catalysts. To determine the catalyst surface temperature during operation under simulated concentrated sunlight, thermocouples have been positioned at various positions on the catalyst as shown in Fig. 2 S in the supplemental material. Due to their placement on top of the catalyst surface the thermocouples get directly irradiated, which impacts the temperature readings. A two-step approach based on calculation and numerical simulation is introduced to recover catalyst surface temperatures through computational modelling and then by comparing calculated temperatures with experimentally observed ones thus validating the computation.

First, the catalyst surface temperature is computed by a model for multi-component transport of reacting ideal gas phase mixtures in porous media [21]. While the detailed modelling approach is beyond the scope of this work, a brief overview is given in Section 3.2.

Second, using the computed value of temperature on the catalyst

surface, the thermocouple temperature equilibrium temperature is calculated by an energy-balance [22] given its optical and thermal properties described in Section 3.1.

3.1. Calculate thermocouple temperature under irradiation

To measure the catalyst surface temperature during operation of the reactor, thermocouples were placed on top of the catalyst coated porous frit and thus took part in thermal energy exchange with the surroundings, especially via irradiation exchange, as illustrated for a single thermocouple in Fig. 7.

The surfaces participating in irradiation exchange are the window underside (0), the thermocouple outer surface (1) and the catalyst surface (2). Heat is transferred to the thermocouple by absorption of radiation coming from the window and from the catalyst coated surface. Heat is transferred to the surrounding surfaces from the thermocouple via emitted thermal radiation and to the surrounding gas stream via convection. The spectral characteristics of the irradiation coming from the solar simulator emitting mostly in the visible spectral range and the thermal emissive radiation from the hot surfaces in the infrared range (IR) are considered. Effective optical properties like the absorptance, reflectance, transmittivity and emissivity for the surfaces participating in the irradiation exchange are calculated by weighting the spectral optical properties by the spectrum emitted by the Xe short arc lamps for the visible and by the black body spectrum at 600 °C for the IR range respectively. To reduce the number of parameters and simplify the calculation, the radiation emanating from the window due to emission was neglected. This was justified, as in experiments temperatures of ca. 220 °C were recorded for the inner window surface, albeit at a position at the edge of the window (cf. Figure S 5, T_10). For comparison, the emitted flux density at 220 °C from a black body accounts for less than 5 % of the typical flux irradiation of 70 kW/m^2. Taking the relatively large values for the maximum uncertainty of the various optical properties shown in Table 1 into account, neglecting the emitted radiation from the window does not add significantly to the uncertainty. Then the equilibrium temperature of the sheathed thermocouple (Surface 1) with Ø1 mm assumed to be homogenous can be obtained by solving Eq. 1 which has been already been simplified by diving both sides by A_1:

$$0 = \dot{Q}_{\mathrm{abs},2} + \dot{Q}_{\mathrm{abs},0} - \dot{Q}_{\mathrm{emit}} - \dot{Q}_{\mathrm{conv}} = \phi_{12}\left(\alpha_1^{\mathrm{IR}}\epsilon_2\sigma T_2^4 + \alpha_1^{\mathrm{vis}}\rho_2^{\mathrm{vis}}\phi_{02}G_0\right) + \alpha_1^{\mathrm{vis}}\phi_{10}G_0 - \epsilon_1\sigma T_1^4 - h_{\mathrm{conv}}(T_1 - \overline{T}_{\mathrm{gas}}) \quad (1)$$

Eq. 1: Steady-state thermal energy balance of thermocouple used to determine its equilibrium temperature.

Here, ϕ_{12} and ϕ_{10} are the view factors, accounting for the fraction of radiation energy from Surface 1 reaching Surface 2 or 0 respectively, divided by the total radiation emanating from Surface 1. Since the thermocouple is cylindrical and thus convex and its surface area is negligible compared to the window and catalyst surfaces it follows $\phi_{12} = \phi_{10} = 0.5$. Table 1 gives an overview of the parameters used to calculate the thermocouple temperature according to Eq. 1.

Table 1
Parameters, typical values and associated uncertainties used in the calculation of the thermocouple temperature.

Parameter	Typical value	Range	Typical standard uncertainty / (max. uncertainty)	Source
G_0 [kW/m^2]	70	40 – 80	2.0 (±5 %)	this work (4.1)
α_1^{vis} [-]	0.57		0.066 (±20 %)	[23]
$\alpha_1^{\mathrm{IR}} = \epsilon_1$ [-]	0.54		0.062 (±20 %)	[24]
α_2^{vis} [-]	0.39		0.045 (±20 %)	this work (2.2.1)
$\alpha_2^{\mathrm{IR}} = \epsilon_2$ [-]	0.56		0.064 (±20 %)	this work (2.2.1)
$\dot{V}_{\mathrm{flow,in}}$ [L$_s$/min]*	3.0	0.34 – 5.6	0.015 (±0.5 % Rd + 0.1 % FS)	Spec.
T_2 [°C]	597	444 – 613	31 (Calc.)	this work (3.2)
T_1 [°C]	681	487 – 697	34 (Calc.)	this work (3.1)

* $p_s = 1.01325$ bar, $T_s = 293.15$ K

All calculated results obtained for the thermocouple and catalyst surface temperatures T_1 and T_2 respectively shown in Table 1, Fig. 8, Fig. 10 correspond to conditions prevalent in the centre of the catalyst coated porous frit. Also, a molar feed ratio of $H_2/CO_2 = 1/1$ was applied in all calculations.

The optical parameters $\alpha_1^{\mathrm{IR}}, \alpha_1^{\mathrm{vis}}, \epsilon_1, \rho_2^{\mathrm{vis}}, \epsilon_2$ are the absorptance of Surface 1 in the IR and visible ranges, its emissivity, the reflectance in the visible, and the emissivity of Surface 2, respectively. Values for the absorptances α_1^{vis} and α_1^{IR} of the thermocouple sheath made of Ni alloy are taken from literature [23] and [24] respectively, where appropriate averages were taken to account for the state of oxidation of the thermocouple surface resulting from exposure to high temperatures over extended periods of time. In particular, the value for $\alpha_1^{\mathrm{vis}} = 0.57$ was obtained by averaging the values from curves 3, 7, 11, 15, 19 and 23 on

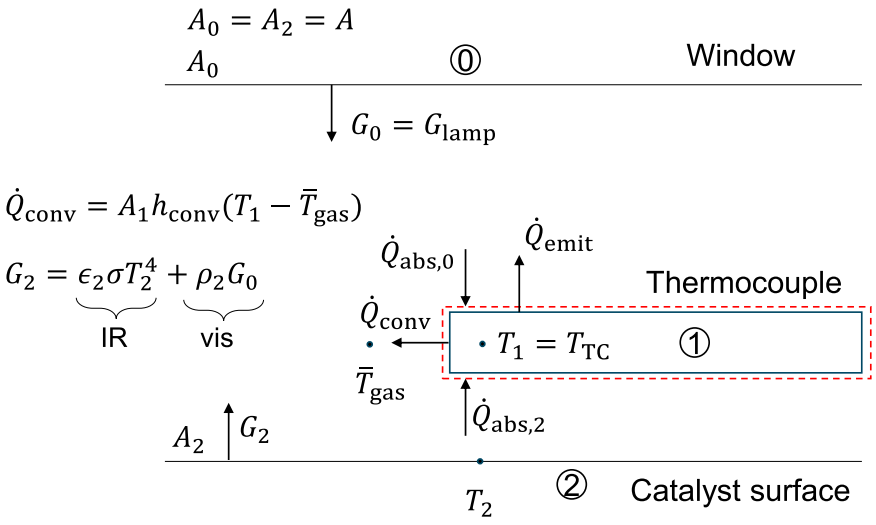

Fig. 7. Schematic sketch of thermocouple and surroundings used to determine the thermocouple energy balance from which its temperature in thermal equilibrium can be calculated.

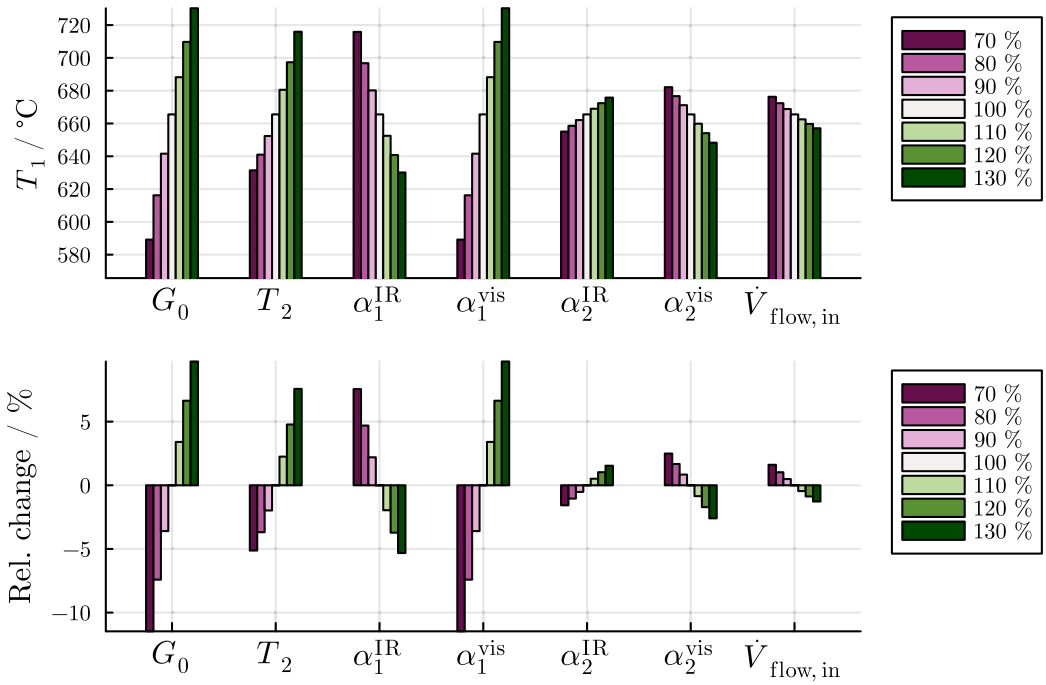

Fig. 8. Exemplary result of OAT sensitivity study of thermocouple temperature (T_1) where the base case of 100 % corresponds to the typical parameter values presented in Table 1.

data table 393. $\alpha_1^{IR} = 0.54$ was obtained by taking the mean of proposed line fits for samples E and D in Table 2–1 at a temperature of 650 °C.

The temperature of the catalyst surface T_2 is calculated from the 3D model and is provided as an input to Eq. 1. The convective heat transfer coefficient h_{conv} is calculated from Nusselt correlation [25] where it is a function of $\dot{V}_{flow,in}$ and T_2. When calculating h_{conv} the gas temperature in these calculations is taken as $\overline{T}_{gas} = (T_2 + T_{gas,in})/2$ the mean of the catalyst surface temperature and the gas inlet temperature, referred to as the film temperature [25].

3.1.1. Sensitivity and uncertainty characterization

Analysing Eq. 1, the functional dependence of the thermocouple temperature T_1 on influencing parameters can be formulated as shown in Eq. 2:

$$T_1 = T_1\left(T_2, G_0, \alpha_1^{vis}, \alpha_1^{IR}, \alpha_2^{vis}, \alpha_2^{IR}, \dot{V}_{flow,in}\right) \quad 2$$

Eq. 2: Functional dependence of the thermocouple temperature T_1 on influencing parameters to be used in sensitivity analysis and uncertainty characterization

An approach to analyse the sensitivity of the result on the input parameters is that of changing one-parameter-at-a-time (OAT) while observing the effect each change of input has on the output. The result of an OAT sensitivity study applied to Eq. 1 is shown in Fig. 8.

Parameter values are varied in the range of −30 % to +30 % around the base value corresponding to the typical parameter values in Table 1. The base case results in thermocouple temperature of 667 °C at a nominal irradiation flux of 70 kW/m^2 and a feed flow of 3 L$_s$/min. The parameters roughly fall in three categories with respect to the sensitivity of the calculation: varying G_0 and α_1^{vis} from −30 % to +30 % both leads to relative changes in T_1 of −11.4 % to +9.7 %. From the standpoint of sensitivity analysis, they could be replaced by their product $G_0\alpha_1^{vis}$ as they only appear together in Eq. 1. The second group consist of the parameters T_2 and α_1^{IR} as their variation impacts the resulting value for T_1 by a similar amount, −5.3 % to 7.8 % and 7.5 % to −5.3 % relative change in output, respectively. It should be pointed out that for α_1^{IR} the sign is inversed as an increase in $\alpha_1^{IR} = \epsilon_1$ leads to a decrease in T_1. The last group of parameters is less significant and comprises $\alpha_2^{vis}, \alpha_2^{IR}$ and $\dot{V}_{flow,in}$ whose variation leads to changes in T_1 of ca. 2.5 % in each direction. Summarising, the irradiation flux G_0 and catalyst surface temperature T_2 are particularly important as well as the optical properties of the thermocouple α_1^{vis} and α_1^{IR} in determining the thermocouple temperature T_1. As the name OAT implies, parameters were varied independently from one another. In reality, T_2 is a function of G_0 and changes upon variation in G_0.

The uncertainty of the calculation result for the thermocouple temperature T_1 as well as the calculated catalyst surface temperature T_2 is assessed via the approach of combined standard uncertainty for uncorrelated input parameters [26] according to Eq. 3.

$$u_c^2 = \sum_{i=1}^{N} \left(\frac{\partial f}{\partial x_i}\right)^2 u^2(x_i) \quad 3$$

Eq. 3: Combined standard uncertainty for uncorrelated input parameters according to the Guide to the expression of uncertainty in measurement (GUM:1995) [26].

To obtain $u_c^2(T_1)$ from Eq. 3 the partial derivatives of $\partial T_1/\partial x_i$ are required which are calculated numerically because Eq. 1 is an implicit function. Also, the variances (squares of standard uncertainties) of the parameters are required which are listed in Table 1. In this work,

a rectangular probability distribution of values around a mean is assumed such the variance of each measurement or parameter subject to uncertainty is calculated as $u^2(x_i) = a^2/3$ where the half-width a is defined as half the difference between the upper and lower bounds a_+ and a_- for the measurement subject to uncertainty, respectively ($a_+ - a_- = 2a$). Because accuracy ratings for the parameters used were often missing estimates for relative accuracy were used e.g. (±5 %) for G_0 as shown in Table 1. Following this approach, a standard combined uncertainty of 33 °C for the thermocouple temperature is obtained for the typical parameter values from Table 1. This approach is also applied for uncertainty characterization in Section 4.

3.2. Detailed modelling of catalyst layer and support

A detailed model for multi-component transport of reacting ideal gas phase mixtures in porous media has been developed [21]. The porous media is described on the basis of the quasi-homogeneous phase approach [27,28]. The multi-component mass transport is described by convective-diffusive transport. The convective contribution comes from the mass averaged velocity calculated from Darcy equation and the diffusive contribution is described by the Maxwell-Stefan multi-component diffusion relations [29,30]. The thermal energy transport considers convective-diffusive transport and is formulated with effective parameters [31] that follow as a consequence of the quasi-homogeneous approach. When the model is applied to the photo-thermal reactor, the modelling domain is restricted to the supported catalyst and the porous frit support, while interaction with the reactor bounding surfaces is accounted for via boundary conditions.

Irradiative heat transport is treated as heat flux boundary conditions on the irradiated areas. Chemical reactions are modelled based on the assumption that the catalyst is activated by temperature and kinetic reaction rate descriptions for steam reforming and water-gas-shift reactions [32] in the field of thermal catalysis are applied. The modelling equations are discretized in three space dimensions and solved with the finite-volume method via the open-source package VoronoiFVM.jl [33] for the julia [34] programming language.

4. Results and discussion

4.1. Flux distribution

The resulting effective flux distribution incident on the catalyst layer upon irradiation with the solar simulator was measured as described in Section 2.3.1. An exemplary result for a nominal flux of 40 kW/m^2 is shown in Fig. 9 where a flux map for the total illuminated area of 12 cm×12 cm was recorded. The core area of 10 cm×10 cm is highlighted where a homogeneous flux profile should be realised. The total effective power incident on the core area amounts to 0.39 kW with minimum, maximum and mean fluxes of 26.3 kW/m^2, 42.6 kW/m^2 and 39.1 kW/m^2 respectively and a standard deviation of 2.3 kW/m^2 or 5.8 % relative to the mean value. The effective irradiative power incident on the total illuminated area of 12 cm×12 cm amounts to 0.51 kW with minimum, maximum and mean fluxes of 4.2 kW/m^2, 42.6 kW/m^2 and 35.6 kW/m^2 respectively and a standard deviation of 6.87 kW/m^2 or 19.3 %.

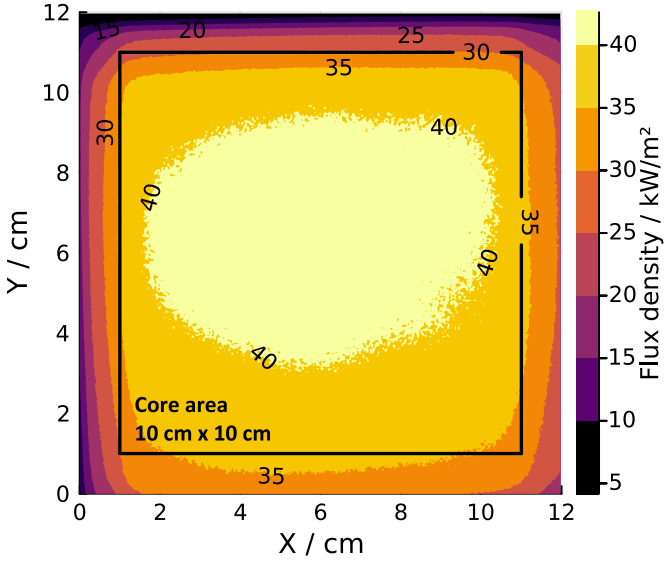

Fig. 9. Exemplary flux map measured on the catalyst plane (nominal flux: 40 kW/m^2 equivalent to 40 suns on catalyst core area of 10 cm×10 cm).

Table 2 shows the effective mean fluxes incident on the core area and total illuminated area for all nominal fluxes considered during the experimental campaign. Additional flux profiles for nominal fluxes of 60, 80 and 100 kW/m^2 are shown in Figures S 7–9 in the supplemental material.

4.2. Reactor operation

The rWGS reaction at a $RuO_2/SrTiO_3$ catalyst in the photo thermal catalytic reactor was investigated under various operation conditions. Besides irradiation conditions (40 to 80 kW/m^2), the flow of the reactants (0.34 to 5.6 L_s/min) as well as the H_2/CO_2 ratio of the feed (0.5/1 to 2/1) were varied. In total the reactor was operated for 45.5 h under simulated concentrated sunlight of which 35.4 h account for operation with a reactant feed of H_2 and CO_2 for chemical operation. All results presented in Section 4.2 refer to experiments conducted with 500 mg catalyst directly deposited on the porous glass frit as outlined in Section 2.2. An overview over reactor geometry, input and operational parameters covered by the experiments is given in Table 3.

4.2.1. Thermal evaluation

Operational experience with the RuO_2-$SrTiO_3$ catalyst introduced in Section 2.2 in laboratory test reactors and in the directly irradiated reactor presented in Section 2.1 and subject to this work indicates that the catalyst activity is predominantly a function of temperature while a photon-driven mechanism could not be confirmed. Thus, to better understand the chemical processes taking place during reactor operation knowledge of local catalyst temperature is indispensable. As outlines in Section 3 the direct measurement of catalyst temperature is complicated through the irradiation incident on the catalyst and subsequently on the thermocouples when placed on the top of the catalyst.

In this section the calculation-based approach presented in Section 3 is validated by comparing calculated with experimentally recorded temperatures from thermocouples placed on top of the catalyst coated porous support. For the calculations of the catalyst surface and thermocouple temperatures the locally prevalent value of irradiation flux, as prescribed by the flux maps, is used. For the centre position corresponding to the position of thermocouple "T_03" (cf. Figure S 5) on the catalyst, Fig. 10 compares the calculated temperatures with experiments under different conditions where the data behind the plots can be found in the supplemental information in Table S 1 and S 2 for Fig. 10 a) and b) respectively.

Specifically, in Fig. 10 a) the comparison is shown for a total feed flow of 3 L_s/min with a molar ratio of $H_2/CO_2 = 1/1$ for nominal irradiation fluxes of in the range of 40 to 70 kW/m^2. It can be seen that the calculated temperature is consistently too high with a mean deviation of about 20 K with a maximum deviation of 24 K at 40 kW/m^2 and a minimum deviation of 18 K at 60 kW/m^2. The experimental points all lie within in the range defined by the standard uncertainty which has a

Table 2
Nominal and effective mean flux on catalyst core area (10 cm x 10 cm) and the illuminated area of 12 cm×12 cm.

Flux on catalyst area in kW/m^2		
Core (10 cm×10 cm)		Illuminated (12 cm×12 cm)
Nominal	Effective	Effective
40	39.1	35.5
45	44.5	40.5
50	49.3	44.9
55	54.2	49.3
60	58.7	53.4
65	62.8	57.2
70	67.2	61.2
75	71.8	65.4
80	76.4	69.6

Table 3
Overview of geometric, input and operational parameters covering the parameter ranges during experimental testing with the catalyst directly applied to a porous frit.

Geometry	MIN	NOMINAL	MAX
Aperture area in cm^2		144	
Catalyst coated area in cm^2		190*	
Catalyst mass loading in mg		500	
Input			
Nominal concentration ratio (centre of catalyst plane, 100 cm^2)	40	70	80
Average concentration ratio (total catalyst plane, 144 cm^2)	35.5	61.2	69.6
Solar power (total catalyst plane) in W	511	881	1002
Solar power (on reactor window) in W	568	979	1114
Total reactant gas flow ($H_2/CO_2 = 1/1$) in mL_s/min*	340	3000	5600
Operating conditions			
Reactor pressure bar_g	0.0	0.1	0.2
Catalyst temperature in °C	400	646	700 **

* 144 cm^2 illuminated main region + barely illuminated but accessible rim region
** limited by the porous glass frit

mean value of 31 K. In Fig. 10 b) a total feed flow of 5.6 L_s/min with a molar ratio of $H_2/CO_2 = 1/1$ for nominal irradiation fluxes of in the range of 40 to 80 kW/m^2 was investigated. Here, the agreement between calculation and experiment is better showing a mean deviation of about 11 K with maximum deviation of 14 K at 70 kW/m^2 and a minimum deviation of 9 K at 80 kW/m^2. Besides the centre, additional thermocouples were placed on the catalyst surface shown in Figure S5. Thus, computations at positions indicated by the respective thermocouples are performed while taking the local value of irradiation flux into account. The results of these computations are contrasted with measurements in Fig. 11. Overall the computation tends to overestimate the thermocouple temperature, as there are more datapoints above the diagonal. This was also the case for the centre position analysed in Fig. 10. The variability in temperature between the different thermocouples for a single operating point can be as big as 70 K. The temperature variations are to a large extend caused by the spatial variation in flux density and highlight the need to take the local irradiation into account when performing calculations. There are however also the thermocouples "T_04" and "T_05" whose values are well matched for all operating conditions. The fact that there is some degree of uncertainty regarding the position of the thermocouple tips as they could not be positively affixed directly to the catalyst should be kept in mind. Fig. 10 and Fig. 11 reveal an overall satisfactory agreement between the calculated and experimental thermocouple temperatures in the considered operating conditions.

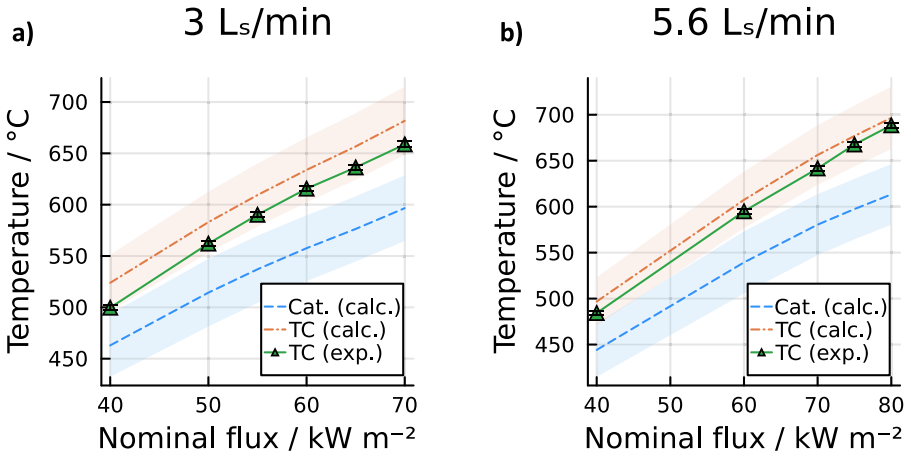

Fig. 10. Calculated catalyst surface temperatures (blue curve), calculated thermocouple temperatures, and experimental thermocouple temperatures in the centre of the frit for total reactant feed flows of a) 3 L_s/min and b) 5.6 L_s/min at $H_2/CO_2 = 1/1$ molar ratio for various irradiation fluxes. The shaded areas for calculated values and error bars for measurements correspond to standard uncertainties.

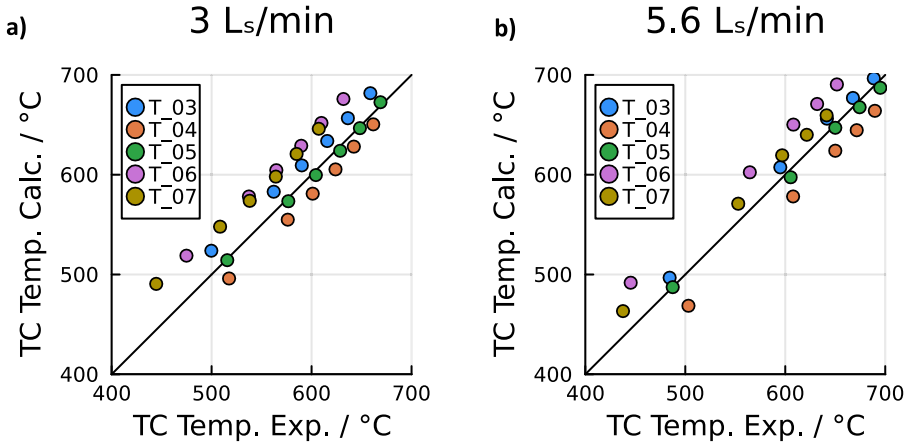

Fig. 11. Parity plots comparing experimentally observed thermocouple temperatures with calculated ones at the positions assigned to the respective thermocouples. The datapoints correspond to operation under nominal irradiation fluxes of a) 40 to 70 kW/m^2 at constant total feed flow rate of 3 L_s/min and b) 40 to 80 kW/m^2 with total flow rate of 5.6 L_s/min at $H_2/CO_2 = 1/1$ molar ratio in a) and b).

However, as was shown in Section 3.1.1 the calculations are very sensitive towards changes in some of the parameters, especially in the value of irradiation flux density. This is reflected by the rather large margins of standard uncertainty in Fig. 10.

This example emphasizes that care should be taken when recording flux density maps and obtaining the parameter values. In the case of optical properties for thermocouple sheath materials, information in the literature is scarce and uncertainties in the measured values are often unquantified. Also, this informs planning for upcoming experimental investigations to implement measures to avoid irradiation effects in temperature measurements e.g. by more sophisticated thermocouple placement. Nevertheless, the calculation-based approach is a valuable tool that supports the understanding of the system and its sensitivity in changes in the operating parameters.

4.2.2. Chemical evaluation

As outlined in Section 2.2, at the outset glass fibre sheets were used as catalyst support, which were loaded with 100 to 200 mg of catalyst. However, deformation and embrittlement of the catalyst coated sheets were observed, which led to a fast degradation of observed reactor performance. Thus, results presented herein refer to experiments, where 500 mg of catalyst were directly deposited onto the porous frit. This reactor configuration was operated under simulated concentrated sunlight at different levels of irradiation flux, total feed gas flow and feed gas compositions. The chosen operating conditions were held constant until stationary reactor operation was reached, leading to a total operation duration of 26.1 h over the course of 8 testing days. An exemplary plot illustrating the time evolution of selected operational quantities at varying operating conditions is shown in Figure S 10 in the supplementary material. Throughout this text, the reported quantities refer to time averaged values obtained during stationary operation, where averaging generally occurred over a minimal duration of 10 minutes.

Fig. 12 summarises all experiments and corresponding experimental conditions with respect to the CO fraction in the dry product gas. In addition, the same data is visualised as separate plots of molar CO fraction in the dry product gas as a function of the nominal irradiation flux, total feed gas flow and feed gas composition, shown in Figures S 11–13 of the supplemental information.

Time-averaged values of CO molar fraction in the dry product gas between 3.3 % and 16.5 % were obtained. In general, good reproducibility can be attested when considering CO molar fraction in the product gas as a proxy for reactor performance e.g. for operating conditions at a total flow rate of 3000 mL_s/min and 40 kW/m^2 and 50 kW/m^2 of nominal irradiation flux density, respectively. The molar fraction of CO increases with flux and decreases with flow of reactants. The considered variation of the feed composition influences the CO fraction by max. 1.1 % points. Good stability was observed during 14.1 h of testing under concentrated irradiation with varying operating conditions over the course of 5 days. A slight decrease of the CO fraction under similar conditions was observed after Day 5 when highest fluxes of 75 to 80 kW/m^2 were applied and highest temperatures were measured.

After this point, a decreasing trend in molar CO fraction in the dry product gas starting from ca. 5 % on Day 6 was observed for three consecutive days. Presumably, the parts of the catalyst and porous support exposed to the largest thermal stress resulting from the high irradiation fluxes were subject to degradation although there was no obvious sign of degradation upon visual inspection. Summarizing, the variation of feed composition showed relatively minor effects and is therefore not considered further. The irradiation flux and feed flow rate were identified as the main operational parameters and are subject to further analysis in the following.

4.2.3. Selectivity and solar-to-chemical efficiency

The developed photo-thermal reactor aims at the conversion of solar irradiation into chemical energy via the endothermic rWGS reaction which was introduced in Section 1. Thus, an appropriate measure for the energetic efficiency of the process considers the energetic change as a result of the chemical reaction occurring in the reactor, the rate of reaction as well as the solar power input necessary to drive the reaction. Therefore, a solar-to-chemical efficiency based on the target product CO (STC_{CO}) for the reactor can be defined based on the change in enthalpy or change in Gibbs free energy of the reverse Water Gas Shift reaction and the solar power input as $STC_{CO}^{\Delta h} = \frac{\dot{n}_{CO} \Delta h^0_{rWGS}}{\dot{Q}_{sol}}$ or $STC_{CO}^{\Delta g} = \frac{\dot{n}_{CO} \Delta g^0_{rWGS}}{\dot{Q}_{sol}}$.

In the calculation of solar-to-chemical efficiency the irradiation flux

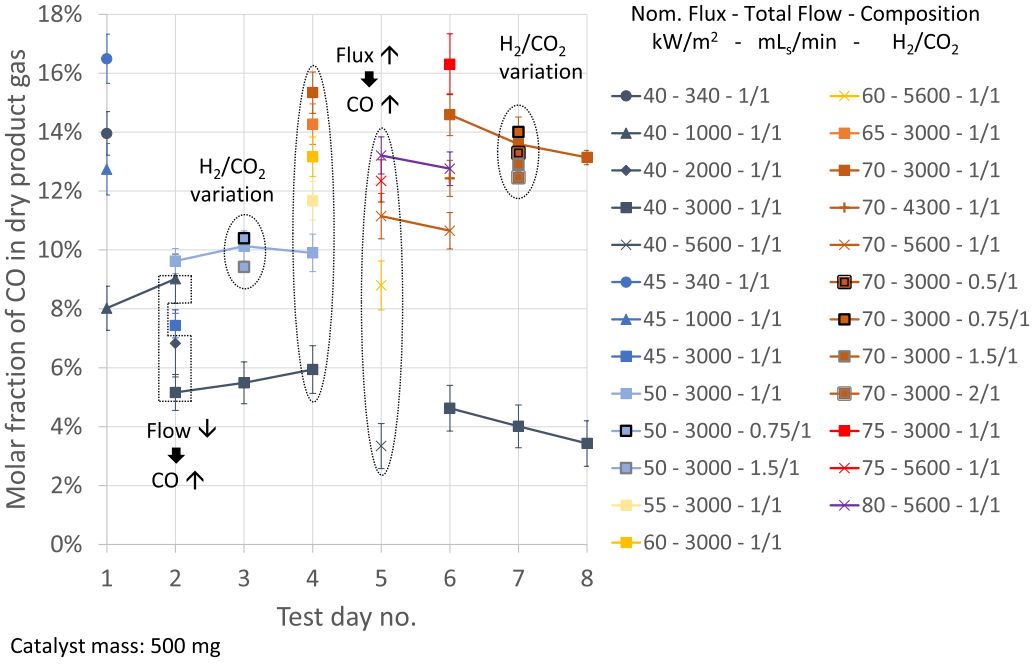

Fig. 12. Molar fractions of CO in dry product gas of the reactor achieved on particular test days as a function of the varied operation conditions: nominal average flux on the core catalyst area, total flow of reactants, and molar composition of reactants (average values if conditions were applied more than once on a test day). Uncertainty indicators refer to standard uncertainty.

incident on the reactor window was used. Since no direct measurement of the irradiation flux incident on the reactor window is available, it is instead computed by integrating the flux distribution measured in the catalyst plane as described in Section 2.3.1 and by accounting for window optical reflection losses of 10 %. Thus, losses occurring in the optical system beyond window reflection losses are not considered in the efficiency calculations.

For the rWGS reaction the change of reaction enthalpy and change of Gibbs free energy of reaction at standard conditions (298.15 K, 1 bar_a) are $\Delta h^0_{rWGS} = 41.2$ kJ/mol and $\Delta g^0_{rWGS} = 28.6$ kJ/mol, respectively. Besides the main product CO, the reactor also produces small amounts of methane (CH_4) as a side product.

For the competing methanation or Sabatier reaction [35]

Sabatier: $CO_2 + 4\ H_2 \rightleftharpoons CH_4 + 2\ H_2O$

the change of enthalpy of reaction and change of Gibbs free energy of reaction at standard conditions are $\Delta h^0_{Sabatier} = -164.7$ kJ/mol and $\Delta g^0_{Sabatier} = -113.3$ kJ/mol, respectively.

Since the Sabatier reaction is energetically downhill ($\Delta h^0_{Sabatier} < 0,\ \Delta g^0_{Sabatier} < 0$) it is relevant from an energetic standpoint to consider the energy release by this unintended reaction in the STC efficiency, for which the following STC_{CO,CH_4} efficiencies are proposed:$STC^{\Delta h}_{CO,CH_4} = \frac{\dot{n}_{CO}\Delta h^0_{rWGS} + \dot{n}_{CH_4}\Delta h^0_{Sabatier}}{\dot{Q}_{sol}}$ or $STC^{\Delta g}_{CO,CH_4} = \frac{\dot{n}_{CO}\Delta g^0_{rWGS} + \dot{n}_{CH_4}\Delta g^0_{Sabatier}}{\dot{Q}_{sol}}$.

Fig. 13 gives an overview over the STC efficiencies and CO selectivities obtained for a representative selection of operating conditions when the STC efficiency is defined based on the change of enthalpy of reaction Δh^0_R and the selectivities towards CO and CH_4, S_{CO} and S_{CH_4}, are defined by:$S_{CO} = \frac{\dot{n}_{CO}}{\dot{n}_{CO}+\dot{n}_{CH_4}}$ and $S_{CH_4} = \frac{\dot{n}_{CH_4}}{\dot{n}_{CO}+\dot{n}_{CH_4}}$, respectively

Fig. 13 comprises experimental results where the total feed flow was varied from 0.34 L_s/min up to 5.6 L_s/min at a fixed ratio of $H_2/CO_2 = 1/1$ while two levels of nominal irradiation fluxes, 40 and 70 kW/m^2 were considered. The effect of including the unintended CH_4 formation on the STC is investigated and contrasted against STC values obtained when only considering the target product CO. Values for S(CO) are high for all considered conditions. For the lower nominal irradiation flux of 40 kW/m^2 a maximum S(CO) of 99 % was obtained at low flow rates slightly decreasing with increasing flowrates to a minimum value of 87 %. For the operating conditions with irradiation flux of 70 kW/m^2 values of S (CO) remained constant at around 96 % for all investigated flow rates.

Values for $STC^{\Delta h}_{CO}$ ranging from 0.21 % to 1.69 % and for $STC^{\Delta g}_{CO}$ from 0.14 % to 1.18 % were obtained.

In general, the STC efficiencies are lower when considering CH_4 formation, the penalty is especially significant when the selectivity towards CH_4 is higher. Also, the values obtained for the STC efficiencies based on Δg^0_R are slightly lower than based on Δh^0_R.

Overall, a trend towards higher STC efficiencies can be observed for higher flux concentrations as well as higher feed flow rates. Increased irradiation fluxes manifest in higher catalyst temperatures which have a positive impact on the rate of reaction and also shift the thermodynamic equilibrium towards increased formation of the target product CO. Increasing the feed flow rate likely leads to improved mass transport between the gas phase and the solid catalyst increasing reactant availability on the active catalyst centres and thus increasing reaction rates and productivity.

Increasing the feed flow rate comes at the expense of lowering the concentration of CO in the product stream, which increases the purification effort downstream of the reactor before utilization of the product stream. Also, increasing the irradiation flux beyond a certain point will lead to issues of thermal stability. Thus, an optimal operating point is a compromise that is informed by the requirements of the downstream processes, where requirements regarding CO productivity and CO concentration in the product stream must be balanced.

A summary of the experimental results obtained during the chemical testing in the arrangement introduced at the outset of Section 4.2.2 is given in Table 4. There minimal, nominal and maximal values for applied irradiation flux density, overall and catalyst mass specific CO generation rate, CO selectivity and yield (CO_2 basis) as well as values for molar fraction in the dry product gas are reported. Also values for the achieved solar-to-chemical efficiency for the different definitions introduced in Section 4.2.3 are given.

5. Conclusions and outlook

In this study a novel photo-thermal reactor designed for atmospheric

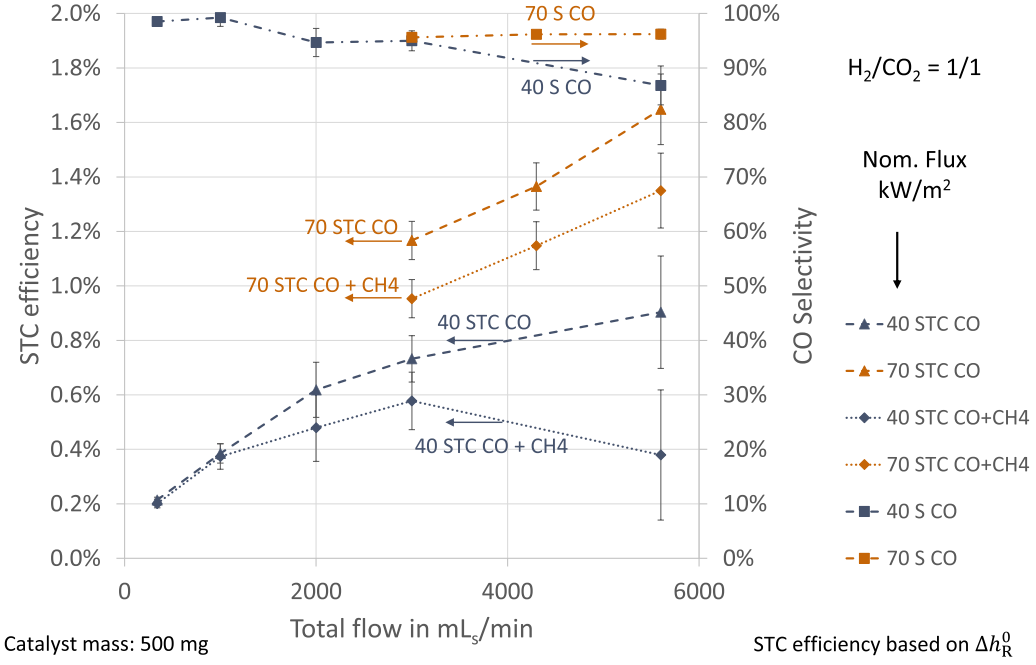

Fig. 13. STC efficiency of the photo-thermal reactor considering the presence of "CO" and "CO+CH4" in the product gas as well as CO selectivity for selected operating conditions as a function of the total flow of reactants and the irradiation conditions. Uncertainty indicators refer to standard uncertainty.

Table 4
Summary of chemical output characteristics observed during experimental testing.

Output	MIN	NOMINAL	MAX
Nom. irradiation flux density in kW/m^2	40	70	80
CO in mol/h	0.11	1.0	1.6
CO generation rate in mol/(h g_{cat})	0.22	2.0	3.2
CO selectivity* in %	84	96	100
CO yield (CO_2 basis) in %	5	27	27
CO molar fraction (dry) in %	3.3	15.3	16.5
STC efficiency (CO) based on Δh_R^0 (Δg_R^0) in %	0.21 (0.14)	1.17 (0.81)	1.69 (1.18)
STC efficiency (CO,CH_4) based on Δh_R^0 (Δg_R^0) in %	0.13 (0.09)	0.95 (0.66)	1.49 (1.04)

* CO selectivity $S_{CO} = \dot{n}_{CO}/(\dot{n}_{CO} + \dot{n}_{CH_4})$.

pressure operation was introduced together with a suitable catalyst and deposition method to perform the rWGS reaction under concentrated solar irradiation in continuous flow. Through experimental testing of the system in a solar simulator with irradiation flux densities of up to 80 kW/m^2 and corresponding total irradiative power input of up to around 1 kW incident on the catalyst over a time period of 35 h of chemical operation it was shown that the proposed system is a viable option to continuously produce CO from CO_2 and H_2. Thus, a proof-of-concept under practical conditions could successfully be obtained. Up to 1.6 mol/h of CO were produced associated with a CO yield of up to 27 %. The CO molar fraction in the product gas reached values as high as 16.5 % and solar-to-chemical efficiencies up to 1.7 % were calculated. The integrity of the reactor components could generally be confirmed. A nominal flux density in the catalyst core area of 70 kW/m^2 could be derived as a reasonable operation limit for this reactor configuration, since it is indicated that – within the range of applied operation conditions – higher flux densities lead to a degradation of the catalyst itself or the porous support structure.

A calculation-based approach was introduced to retrieve catalyst surface temperatures during operation which proved as a valuable tool to gain additional understanding about the system while at the same it is subject to potentially large uncertainties introduced by the model parameters. This motivates the development of more sophisticated techniques of thermocouples placement to measure the catalyst surface temperature while avoiding direct irradiation exposure.

The comprehensive understanding of the reactor and its operation characteristics gained in the reported experiments and the model-based calculation of the effective catalyst temperature represent an excellent basis for upcoming improvement steps, which aim at increasing the solar-to-chemical efficiency and CO molar fraction in the product gas.

CRediT authorship contribution statement

David Brust: Writing – original draft, Visualization, Validation, Software, Formal analysis. **Hermenegildo García Gómez:** Funding acquisition, Conceptualization. **Michael Wullenkord:** Writing – review & editing, Visualization, Validation, Supervision, Project administration, Methodology, Funding acquisition, Conceptualization. **Christian Sattler:** Writing – review & editing, Resources. **Josep Albero:** Writing – original draft, Visualization, Project administration, Conceptualization.

Declaration of Competing Interest

The authors declare that they have no known competing financial interests or personal relationships that could have appeared to influence the work reported in this paper.

Data availability

Data will be made available on request.

Acknowledgements

The authors would like to thank the DLR team for their support and for the realisation of optics (C. Willsch, G. Dibowski) and test setup (M. Kloft, C. Spenke) and data acquisition and control (K. Eßer, F. Pierno). Also, the authors acknowledge funding from the European Union's Horizon 2020 Research and Innovation Programme under grant agreement No 862453. The material presented and views expressed here are the responsibility of the authors only. The EU Commission takes no responsibility for any use made of the information set out.

The help on part of PCM-OTP CNRS PROMES in performing the opto-thermal spectral measurements (C. Escape) is appreciated. This work was supported by the French "Investments for the future" programme managed by the National Agency for Research under contract ANR-10-EQPX-49-SOCRATE.

J.A. thanks the Spanish Ministry of Science and Innovation for the Ramon y Cajal research associate contract (RYC2021-031006-I financed support by MCIN/AEI/10.13039/501100011033 and by European Union/NextGenerationEU/ PRTR) and the financial support (PID2022–141099OA-I00 funded by MCIN/AEI/10.13039/501100011033 and FEDER "Una manera de hacer Europa".

Appendix A. Supporting information

Supplementary data associated with this article can be found in the online version at doi:10.1016/j.jece.2024.113372.

References

[1] IPCC, Summary for Policymakers, in: V. Masson-Delmotte, P. Zhai, A. Pirani, S. L. Connors, C. Péan, S. Berger, N. Caud, Y. Chen, L. Goldfarb, M.I. Gomis, M. Huang, K. Leitzell, E. Lonnoy, J. Matthews, T.K. Maycock, T. Waterfield, O. Yelekçi, R. Yu, B. Zhou (Eds.), Climate Change 2021: The Physical Science Basis. Contribution of Working Group I to the Sixth Assessment Report of the Intergovernmental Panel on Climate Change, Cambridge University Press, Cambridge, United Kingdom and New York, NY, USA, 2021, pp. 3–32.
[2] W.F. Lamb, T. Wiedmann, J. Pongratz, R. Andrew, M. Crippa, J.G.J. Olivier, D. Wiedenhofer, G. Mattioli, A.A. Khourdajie, J. House, S. Pachauri, M. Figueroa, Y. Saheb, R. Slade, K. Hubacek, L. Sun, S.K. Ribeiro, S. Khennas, S. de La Rue Can, L. Chapungu, S.J. Davis, I. Bashmakov, H. Dai, S. Dhakal, X. Tan, Y. Geng, B. Gu, J. Minx, A review of trends and drivers of greenhouse gas emissions by sector from 1990 to 2018, Environ. Res. Lett. 16 (2021), https://doi.org/10.1088/1748-9326/abee4e.
[3] J. Zhang, H. Chen, X. Duan, H. Sun, S. Wang, Photothermal catalysis: from fundamentals to practical applications, Mater. Today 68 (2023) 234–253, https://doi.org/10.1016/j.mattod.2023.06.017.
[4] K. Lorber, P. Djinović, Accelerating photo-thermal CO2 reduction to CO, CH4 or methanol over metal/oxide semiconductor catalysts, iScience 25 (2022) 104107, https://doi.org/10.1016/j.isci.2022.104107.
[5] J. Artz, T.E. Muller, K. Thenert, J. Kleinekorte, R. Meys, A. Sternberg, A. Bardow, W. Leitner, Sustainable conversion of carbon dioxide: an integrated review of catalysis and life cycle assessment, Chem. Rev. 118 (2018) 434–504, https://doi.org/10.1021/acs.chemrev.7b00435.
[6] P.W. Andreas Jess, Chemical Technology: an Integral Textbook, Wiley-VCH, 2013.
[7] Y. Izumi, Recent advances in the photocatalytic conversion of carbon dioxide to fuels with water and/or hydrogen using solar energy and beyond, Coord. Chem. Rev. 257 (2013) 171–186, https://doi.org/10.1016/j.ccr.2012.04.018.
[8] Ž. Kovačič, B. Likozar, M. Huš, Photocatalytic CO2 reduction: a review of ab initio mechanism, kinetics, and multiscale modeling simulations, ACS Catal. 10 (2020) 14984–15007, https://doi.org/10.1021/acscatal.0c02557.
[9] F. Zhang, Y.-H. Li, M.-Y. Qi, Y.M.A. Yamada, M. Anpo, Z.-R. Tang, Y.-J. Xu, Photothermal catalytic CO2 reduction over nanomaterials, Chem. Catal. 1 (2021) 272–297, https://doi.org/10.1016/j.checat.2021.01.003.
[10] G. Baffou, R. Quidant, Nanoplasmonics for chemistry, Chem. Soc. Rev. 43 (2014) 3898–3907, https://doi.org/10.1039/c3cs60364d.
[11] A.A. Upadhye, I. Ro, X. Zeng, H.J. Kim, I. Tejedor, M.A. Anderson, J.A. Dumesic, G. W. Huber, Plasmon-enhanced reverse water gas shift reaction over oxide supported Au catalysts, Catal. Sci. Technol. 5 (2015) 2590–2601, https://doi.org/10.1039/c4cy01183j.
[12] P. Martínez Molina, N. Meulendijks, M. Xu, M.A. Verheijen, T. Hartog, P. Buskens, F. Sastre, Low temperature sunlight-powered reduction of CO 2 to CO using a

plasmonic Au/TiO2 nanocatalyst, ChemCatChem (2021), https://doi.org/10.1002/cctc.202100699.
[13] P. Martinez Molina, K.W. Bossers, J.D. Wienk, J. Rohlfs, N. Meulendijks, M. A. Verheijen, P. Buskens, F. Sastre, Sunlight powered continuous flow reverse water gas shift process using a plasmonic Au/TiO2 nanocatalyst, Chem. Asian J. (2023) e202300405, https://doi.org/10.1002/asia.202300405.
[14] J. Volders, K. Elen, A. Raes, R. Ninakanti, A.S. Kelchtermans, F. Sastre, A. Hardy, P. Cool, S.W. Verbruggen, P. Buskens, M.K. van Bael, Sunlight-powered reverse water gas shift reaction catalysed by plasmonic Au/TiO2 nanocatalysts: effects of Au particle size on the activity and selectivity, Nanomaterials 12 (2022), https://doi.org/10.3390/nano12234153.
[15] L. Wang, Y. Dong, T. Yan, Z. Hu, A.A. Jelle, D.M. Meira, P.N. Duchesne, J.Y.Y. Loh, C. Qiu, E.E. Storey, Y. Xu, W. Sun, M. Ghoussoub, N.P. Kherani, A.S. Helmy, G. A. Ozin, Black indium oxide a photothermal CO2 hydrogenation catalyst, Nat. Commun. 11 (2020) 2432, https://doi.org/10.1038/s41467-020-16336-z.
[16] D. Lou, Z. Zhu, Y.-F. Xu, C. Li, K. Feng, D. Zhang, K. Lv, Z. Wu, C. Zhang, G.A. Ozin, Le He, X. Zhang, A core-shell catalyst design boosts the performance of photothermal reverse water gas shift catalysis, Sci. China Mater. 64 (2021) 2212–2220, https://doi.org/10.1007/s40843-020-1630-2.
[17] D. Mateo, J. Albero, H. García, Titanium-perovskite-supported RuO2 nanoparticles for photocatalytic CO2 methanation, Joule 3 (2019) 1949–1962, https://doi.org/10.1016/j.joule.2019.06.001.
[18] S. Caron, M. Farchado, G. San Vicente, A. Morales, J. Ballestrín, M.J. Carvalho, S. Pascoa, E. Le Baron, A. Disdier, E. Guillot, C. Escape, J.-L. Sans, Y. Binyamin, M. Baidossi, F. Sutter, M. Röger, F. Manzano-Agugliaro, Intercomparison of opto-thermal spectral measurements for concentrating solar thermal receiver materials from room temperature up to 800 °C, Sol. Energy Mater. Sol. Cells 266 (2024) 112677, https://doi.org/10.1016/j.solmat.2023.112677.
[19] G. Dibowski, A. Neumann, P. Rietbrock, C. Willsch, Säck, Jan-Peter und Funken, Karl-Heinz, Der neue Hochleistungsstrahler des DLR - Grundlagen, Technik, Anwendung, Köln, 2007.
[20] M. Thelen, C. Raeder, C. Willsch, G. Dibowski, A high-resolution optical measurement system for rapid acquisition of radiation flux density maps, AIP Conf. Proc. (2017) 1850, https://doi.org/10.1063/1.4984534.
[21] D. Brust, K. Hopf, J. Fuhrmann, A. Cheilytko, M. Wullenkord, C. Sattler, Transport of heat and mass for reactive gas mixtures in porous media: modeling and application, Preprint (2024), https://doi.org/10.2139/ssrn.4789285.
[22] V. Hindasageri, R.P. Vedula, S.V. Prabhu, Thermocouple error correction for measuring the flame temperature with determination of emissivity and heat transfer coefficient, Rev. Sci. Instrum. 84 (2013) 24902, https://doi.org/10.1063/1.4790471.
[23] Y.S. Touloukian, D.P. DeWitt, Thermal radiative properties metallic elements and alloys [by] Y.S. Touloukian [and] D.P. DeWitt, Plenum, New York (1970).
[24] R. Shurtz, Total Hemispherical Emissivity of Metals Applicable to Radiant Heat Testin (2018).
[25] T.L. Bergman, A.S. Lavine, Fundamentals of Heat and Mass Transfer, eighth ed., John Wiley & Sons, Hoboken, NJ, 2017.
[26] Uncertainty of measurement: Guide to the Expression of Uncertainty in Measurement. (GUM:1995), first ed., 2008.
[27] C. Stegehake, J. Riese, M. Grünewald, Modeling and validating fixed-bed reactors: a state-of-the-art review, ChemBioEng Rev. 6 (2019) 28–44, https://doi.org/10.1002/cben.201900002.
[28] VDI Heat Atlas, second ed., Springer Berlin Heidelberg2010..
[29] G.D.C. Kuiken, Thermodynamics of Irreversible Processes: Applications to Diffusion and Rheology, Wiley, New York, NY, 1994.
[30] V. Giovangigli, Multicomponent Flow Modeling, Birkhäuser, Boston, Basel, Berlin, 1999.
[31] P. Zehner, E.U. Schlünder, Wärmeleitfähigkeit von Schüttungen bei mäßigen temperaturen, Chem. Ing. Tech. 42 (1970) 933–941, https://doi.org/10.1002/cite.330421408.
[32] J. Xu, G.F. Froment, Methane steam reforming, methanation and water-gas shift: I. Intrinsic kinetics, AIChE J. 35 (1989) 88–96, https://doi.org/10.1002/aic.690350109.
[33] J. Fuhrmann, contributors, VoronoiFVM.jl: Finite Volume Solver for Coupled Nonlinear Partial Differential Equations, 2019.
[34] J. Bezanson, A. Edelman, S. Karpinski, V.B. Shah, Julia: A fresh approach to numerical computing, SIAM Rev. 59 (2017) 65–98, https://doi.org/10.1137/141000671.
[35] M. Ghoussoub, M. Xia, P.N. Duchesne, D. Segal, G. Ozin, Principles of photothermal gas-phase heterogeneous CO2 catalysis, Energy Environ. Sci. 12 (2019) 1122–1142, https://doi.org/10.1039/c8ee02790k.